



A rGO-Based Fe₂O₃ and Mn₃O₄ binary crystals nanocomposite additive for high performance Li–S battery

Hang Zhang, Qiuming Gao*, Zeyu Li, Peng Xu, Hong Xiao, Tengfei Zhang, Xiao Liang

Key Laboratory of Bio-inspired Smart Interfacial Science and Technology of Ministry of Education, Beijing Advanced Innovation Center for Biomedical Engineering, School of Chemistry, Beihang University, Beijing, 100191, PR China

ARTICLE INFO

Article history:

Received 30 January 2020

Received in revised form

11 March 2020

Accepted 14 March 2020

Available online 18 March 2020

Keywords:

Binary crystals nanocomposite

Additive

Li–S battery

High specific area

High performance

ABSTRACT

Chemical anchor effect is an efficient route for polysulfides immobilization to enhance the performance of Li–S battery. Transition metal oxides are suitable chemical anchor matrix as Lewis acid coordinated with sulfur atoms in the form of Lewis base. Ion bonds may also be formed between anions in transition metal compounds and lithium ions in lithium polysulfides alleviating the shuttle effect. Reducing their crystal sizes to expose more surface active sites and expand surface areas is pivotal to sufficiently immobilize polysulfides. Here, an optimized GFM-2 composite was fabricated, where the 20 nm metal oxide particles aggregated by the 3–5 nm Fe₂O₃ and Mn₃O₄ binary crystals are uniformly distributed on the reduced graphene oxide (rGO) nanosheets. A high specific surface area up to 144.9 m² g^{−1} was obtained for the GFM-2. The modified sulfur@rGO (S@G) cathode obtained by mixing S@G and GFM-2 additive with the mass ratio of 20: 1, presented high specific discharge capacities of 1356.3 and 770.2 mAh g^{−1}, respectively, at scan rates of 0.1 and 5C (1C = 1675 mAh g^{−1}) under conventional electrolyte dosage with electrolyte/sulfur (E/S) = 30 mL g^{−1} and sulfur loading of 1.1 mg cm^{−2}. The capacity was 1053.5 mAh g^{−1} at 1C and maintained at 530.1 mAh g^{−1} after 1000 cycles with the low average capacity decay rate of each cycle of 0.049%. Under low electrolyte dosages of E/S = 15 and 8 mL g^{−1}, the high capacities of 1308.0 and 1230.4 mAh g^{−1} could be still obtained at 0.1C, respectively. When the sulfur loading was increased to 2.8 mg cm^{−2} and E/S was reduced to 10 mL g^{−1}, the good capacity of 1163.6 mAh g^{−1} was gotten at 0.1C. The high capacity and high cyclic property under different E/S and sulfur loading amounts indicate the potential for practical application of this simple but effective modified sulfur cathode.

© 2020 Elsevier Ltd. All rights reserved.

1. Introduction

Lithium-sulfur (Li–S) battery is becoming the most promising secondary energy storage system for the next generation high-performance power units to meet the needs of electric vehicles and other electric driving equipment because of the advantages of high theoretical specific capacity (1675 mAh g^{−1}) and energy density (2600 Wh kg^{−1}) [1–3]. Meanwhile, the active material sulfur possesses the superior characteristics of abundant reserves, low cost and environment-friendly, which are advantageous for large-scale application of the Li–S battery system based on the lithium and sulfur redox reaction for energy storage and release [4–6]. Nevertheless, some problems are urgent to solve in the

future practical Li–S battery system, such as low bulk electronic conductivities in sulfur and its discharging final products Li₂S₂/Li₂S as well as the large volume change of material during electrode reaction which can be remitted by introducing carbon-based materials of porous carbons [7,8], carbon hollow structures [9,10], carbon nanofibers [11,12], carbon nanotubes [13,14], graphenes [15,16], and so forth [17,18]. However, the most critical problem shuttle effect of lithium polysulfides, i.e., the intermediate products in the charging and discharging processes, has not been thoroughly solved, resulting in the loss of active materials and capacity degradation for the Li–S batteries.

Carbon-based materials exhibit advanced performances in conductivity, large specific surface area and structural stability. As the matrixes of electrodes, they can result in good distribution of sulfur materials and fully contact with the carrier materials, which short the transmission path of electrons in sulfur granular phase and contribute to fast electron exchange. The existences of carbon

* Corresponding author.

E-mail address: qmgao@buaa.edu.cn (Q. Gao).

shells may inhibit the escapes of dissolved lithium polysulfides by physical shielding effect [19,20]. However, the non-polarity of C–C bonds make it difficult to form stronger chemical bonds with sulfur atoms [21,22]. Apart from a few specially designed carbon-based materials [23–25], the improvements for the performances of cathode materials by physical inhibition are limited. Therefore, more effective sulfur immobilization strategies are needed.

Transition metal ions possessing of empty d-orbitals and the ability to accept lone pairs of electrons, can be used as Lewis acid to form coordination bonds with sulfur atoms which can provide lone pairs of electrons as Lewis base. Ion bonds may be also formed through anions in transition metal compounds with lithium ions in lithium polysulfides [26–28], which can fix lithium polysulfides with strong chemical bonding force thus reducing the shuttle effect. Nevertheless, transition metal compounds often exhibit the disadvantages of high bulk density, small specific surface area and low electron conductivity. It is necessary to construct small-sized materials with more chemical immobilizing active sites [29–31], and/or to select the materials with relatively high conductivity, e.g., Co_9S_8 and so on [32]. Recently, the composites of graphene and transition metal oxides were reported [33–35], which showed good electrochemical performances due to the sufficient sulfur loading spaces, good electron transport capacities, and effective chemical interactions with sulfur inhibiting the shuttle effect.

Considering the lost-cost, non-poisonous, abundant as well as different impacts of transition metal iron and manganese elements caused by the different reaction mechanisms with graphene oxide (GO) nanosheets (which will be shown later), in this work, the composites of reduced graphene oxide (rGO) nanosheets combined by $\text{Fe}_2\text{O}_3/\text{Mn}_3\text{O}_4$ binary metal oxide nanocrystals (GFM) were prepared by simple liquid phase reaction and subsequent heat treatment at relatively low temperatures using GO, $\text{FeCl}_3 \cdot 6\text{H}_2\text{O}$ and KMnO_4 as the reaction sources. In the structure of the optimized GFM-2 composite, the well dispersed 20 nm particles composing of 3–5 nm $\text{Fe}_2\text{O}_3/\text{Mn}_3\text{O}_4$ binary metal oxide crystals were uniformly distributed on the rGO nanosheets. A high specific surface area of $144.9 \text{ m}^2 \text{ g}^{-1}$ was obtained for the GFM-2. Using as the additive of Li–S battery cathode, the sulfur/rGO (S/G) cathode mixed with a small amount of GFM-2 could deliver high specific capacities of 1356.3 and 770.2 mAh g^{-1} , respectively, at scan rates of 0.1 and 5C ($1\text{C} = 1675 \text{ mAh g}^{-1}$), respectively, under the electrolyte dosage of electrolyte/sulfur (E/S) = 30 $\text{mL g}_\text{S}^{-1}$ and sulfur loading of 1.1 mg cm^{-2} . The mixed cathode is cyclic stable. Even if under the low electrolyte dosages of $\text{E/S} = 15$ and 8 $\text{mL g}_\text{S}^{-1}$, the high capacities of 1308.0 and 1230.4 mAh g^{-1} can be obtained at 0.1C, respectively. When the sulfur loading is increased to 2.8 mg cm^{-2} and E/S is reduced to 10 $\text{mL g}_\text{S}^{-1}$, the capacity can still reach 1163.6 mAh g^{-1} at 0.1C. Thus, a low content of rGO-based binary Fe_2O_3 and Mn_3O_4 composite additive may contribute to a significant high-performance of Li–S battery, presenting the potential for practical application of this simple and effective modified sulfur cathode.

2. Experimental

2.1. Preparation of the samples

GO used in this work was synthesized *via* modified Hummers' method and dissolved in deionized water with ultrasonic treatment to form a 2 mg mL^{-1} solution. In a typical fabrication process for the GFM composites, 1 mmol of $\text{FeCl}_3 \cdot 6\text{H}_2\text{O}$ and 1 mmol of KMnO_4 were added into a 250 mL round bottom flask with 50 mL of water. After totally dissolved, 50 mL of GO solution was added into the flask drop by drop under stirring. The mixed solution was kept reacting at 95°C for 3 h in oil bath with efflux equipment after ultrasonic treatment for 0.5 h. The dark product was separated by

centrifugation and washed with deionized water. After freeze-dried, it was heated to 350°C in Ar gas for 1 h and naturally cooled down to room temperature to obtain the GFM composites. For the optimization, the molar ratio of Fe to Mn in initial materials was adjusted to 3: 1, 1: 1 and 1: 3, respectively, while maintaining the total molar number to 2 mmol, and the corresponding GFM composites obtained were noted as GFM-1, -2 and -3, respectively. Other two groups of contrast samples were set up as rGO nanosheets modified by single one kind of metal oxide, *i.e.*, in the preparation of metal ion solution, 2 mmol of $\text{FeCl}_3 \cdot 6\text{H}_2\text{O}$ or KMnO_4 were dissolved instead of the mixed solution, meanwhile, other conditions were unchanged. The products obtained were noted as GF or GM, respectively.

rGO was obtained by heat-reducing the GO at 800°C in Ar for 1 h. Sulfur and rGO were mixed with the mass ratio of 3: 1 and grinded in agate mortar. The mixture was transferred into fixed kettle and treated at 155°C for 8 h and the S@G composite was obtained.

2.2. Characterization

The morphologies of the materials were observed by field emission scanning electron microscopy (SEM; JSM-7500F; test acceleration voltage 20 kV, experimental current 10 μA) and transmission electron microscopy (TEM; HT7700; acceleration voltage 120 kV). The further characterization of the sample lattice structure was carried out by high resolution transmission electron microscopy (HRTEM; JEM-2100F), and the acceleration voltage is 200 kV. The element distribution of the composite was obtained by energy dispersive X-ray spectrum characterization (EDXS; JEM-2100F). X-ray diffraction (XRD) spectra were measured by Labx XRD-6000 X-ray diffractometer (Shimadzu, Japan). The X-ray was inspired by K_α ray (wavelength: 0.15468 nm). The scanning range was $10\text{--}80^\circ$ and scanning rate was 6° min^{-1} . Thermogravimetric analysis (TGA) was tested on SDTQ600 analyzer in air environment from room temperature to 500°C . N_2 adsorption/desorption curves were measured by American Micromeritics ASAP 2010 specific surface area analyzer at 77 K. The specific surface area was calculated by Brunauer-Emmett-Teller (BET) method. The pore size distribution was analyzed by Density Functional Theory (DFT). Raman spectroscopy was tested by LabRAM HR800 laser confocal Raman spectrometer. The laser wavelength was 532 nm. The X-ray photoelectron spectroscopy (XPS) was tested with K-alpha 1063 equipment (Al K_α ray source).

2.3. Electrochemical measurements

The electrode was prepared by mixing the S@G composite with the GFM series composite additive, conductive carbon black and polyvinylidene fluoride at a mass ratio of 20: 1: 2: 2. After grinding, NMP was added as dispersant to form uniform slurry. Aluminum foil was used as current collector after washed by ethanol. The slurry was spread onto Al foil and dried at 60°C in a vacuum oven for 12 h. Small round plates were cut with diameter of 12 mm and pressed to be used as the cathode electrode. The sulfur loading on electrode was controlled as 1.1 and 2.8 mg cm^{-2} , respectively.

3. Results and discussion

3.1. Synthesis process and structure characterization of the GFM composites

The GO precursor was chosen for synthesis of the GFM composites (Fig. 1), which was reacted with $\text{FeCl}_3 \cdot 6\text{H}_2\text{O}$ and KMnO_4 as follows:

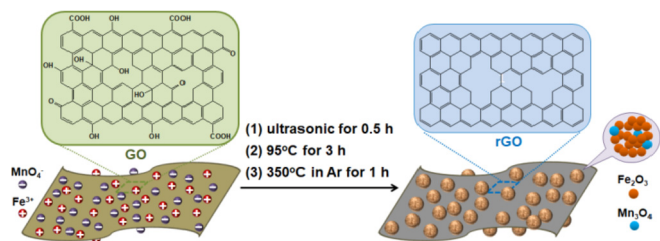
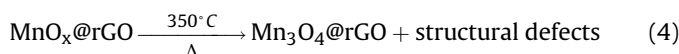
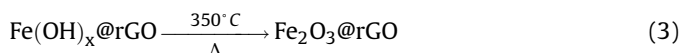
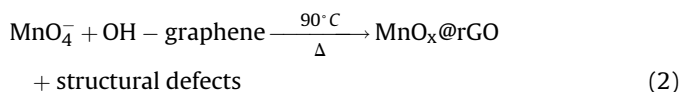
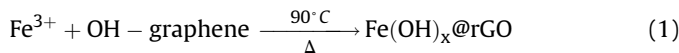


Fig. 1. The schematic synthesis process and related structures of the GFM series composites.



The surface of the GO sheets is rich in structural defects as well as oxygen-containing functional groups such as hydroxyl groups, carboxyl groups and oxygen bridges in the honeycomb-type carbon atom skeleton (OH-graphene) due to the chemical oxidation. The lamellar topologic structure of GO with the structural defects may lead to its relatively large specific surface area. The functional groups make the rGO surface electronegative and easy to adsorb Fe^{3+} ions. Ultrasound treatment can promote their more uniform distribution. During the subsequent 90°C reaction, the iron ions hydrolyzed to form hydroxides ($\text{Fe}(\text{OH})_x @ \text{rGO}$, reaction 1). At the same time, KMnO_4 in the solution reacted with GO under the heating conditions forming the manganese oxides ($\text{MnO}_x @ \text{rGO}$, reaction 2) with formation of some structural defects (pores) based on the redox reaction [36,37]. The relatively large specific surface area of the GO sheets and the pre-dispersion treatments ensure that the metal oxides nanoparticles distributed uniformly on the lamellar surface. In the subsequent heat treatment processes, the iron hydroxides were converted to Fe_2O_3 ($\text{Fe}_2\text{O}_3 @ \text{rGO}$, reaction 3), while manganese oxides existed in the form of Mn_3O_4 ($\text{Mn}_3\text{O}_4 @ \text{rGO}$, reaction 4) with formation of more structural defects. Further growth of the $\text{Fe}_2\text{O}_3/\text{Mn}_3\text{O}_4$ nanocrystals was inhibited since the reaction temperature was relatively low, i.e., 350°C for formation of the GFM series composites.

XRD measurements were used to characterize the GFM series materials (Fig. 2a). Sharp 2θ peaks corresponding to the iron and manganese oxides both appeared for the GFM series samples, indicating effective loading of the metal oxides. The wide 2θ peaks at around 24° is due to the (002) crystal plane of carbon, showing the effective retention of graphene skeleton for the GFM series samples [38,39]. For the rGO combined by Fe_2O_3 (GF) materials, the peaks of oxide in the XRD patterns can be completely consistent with the hematite-type Fe_2O_3 crystals (PDF#33–0664). Correspondingly, the peaks of oxide in the XRD patterns of the rGO combined by Mn_3O_4 (GM) material may be attributed to the hausmannite-type Mn_3O_4 crystals (PDF#24–0734). With adjustment of Fe/Mn ratios in the GFM series composites, the corresponding peaks of the $\text{Fe}_2\text{O}_3/\text{Mn}_3\text{O}_4$ compounds showed regularity of strength increase and decrease separately, indicating

synchronous change of the product compositions caused by adjustment of the raw materials ratios. For the optimized GFM-2 composite, the peak strength of Mn_3O_4 was obviously weak and that of Fe_2O_3 was strong, meaning that the content of Mn_3O_4 is low and that of Fe_2O_3 is high in the composite.

Raman spectra were determined and the curves for the GFM series composites in the range of $100\text{--}1000\text{ cm}^{-1}$ are given in Fig. 2b. The bands of Fe_2O_3 appeared at 215 , 277 and 384 cm^{-1} , corresponding to the vibration responses of $\text{A}_{1g}(1)$, $\text{E}_{2g} + \text{E}_{3g}$ and E_{4g} of Fe–O bonds, respectively [40,41]. While the band of Mn_3O_4 appeared at 650 cm^{-1} corresponding to the stretching vibration response of Mn–O bonds [42,43]. The co-existence of Fe_2O_3 and Mn_3O_4 can be further proved. Coincident with the XRD results, the corresponding band strengths of the two oxides increase or decrease along with the change of their contents, once again certifying that the adjustment of the raw materials ratios can effectively regulate the corresponding product compositions.

N_2 adsorption/desorption isotherms and the pore size distribution curves of GFM-2 are given in Fig. 2c. A typical type-IV isotherm with a small H3-type hysteresis loop could be observed, showing its hierarchical pore texture character. A strong adsorption in low pressure region ($P/P_0 < 0.02$) corresponds to the abundant microporous structure in the composite. The continued increased adsorption at $P/P_0 = 0.02\text{--}0.5$ as well as the hysteresis loop in desorption process in the medium pressure region with P/P_0 at about 0.5 indicates that there are a certain amount of mesopores in the composite. The adsorption in high pressure region is weak, presenting that the macropore in the composites is seldom [44,45]. The pore size distribution curve further illustrates the hierarchical micro/mesopore texture character. The composite exhibits parts of micropores distributed in the range of $0.7\text{--}0.8\text{ nm}$ and more micropores distributed in the range of $1\text{--}2\text{ nm}$. The mesopores are mainly distributed in the range of $2\text{--}5\text{ nm}$, while the macropore is less from the pore distribution. The abundant micropores and a small amount of mesopores make the composite suitable for adsorbing lithium polysulfides. The specific surface area of GFM-2 is up to $144.9\text{ m}^2\text{ g}^{-1}$, meaning that the active surfaces of small-sized oxide crystals in the composite material were adequately exposed, so as to maximize the chemical bonding capability for lithium sulfides. The mass ratio of rGO to metal oxides in GFM-2 was determined by TGA (Fig. 2d). During the calcination in air atmosphere, the mass of the composites began to decay obviously at 250°C , which corresponds to the combustion loss of graphene skeleton since Fe_2O_3 and Mn_3O_4 are stable under this condition. Therefore, the final mass loss of 21.3 wt% is the content of rGO in the GFM-2 composite.

The morphologies of GFM-2 were observed by SEM (Fig. 3a and d). Compared with the basically known ultrathin graphene nanosheets possessing of smooth surface and obvious fold morphology, the surface smoothness of GFM-2 decreased, and the thickness of the sheets increased significantly. There were uniform and dense oxide nanoparticles with sizes of about 20 nm on the surface of graphenes. These phenomena are further proved by the TEM image analyses (Fig. 3b and e). The composite retained the lamellar structure of the graphene nanosheets, but its characteristic fold-layer morphology basically disappeared, indicating that oxide nanoparticles uniformly growing on the surface of the lamellar layers provide certain structural support strength. The layer structure with a certain uniform thickness indicates the growth and uniform distribution of $\text{Fe}_2\text{O}_3/\text{Mn}_3\text{O}_4$ nanocrystals on the surface. Such a structure not only helps to increase the effective contact area between the metal oxide nanocrystals and active materials, but also shortens the electron transport path, so that the electronic exchange between graphene skeleton and lithium polysulfides adsorbed on the metal oxide nanoparticles can be completed

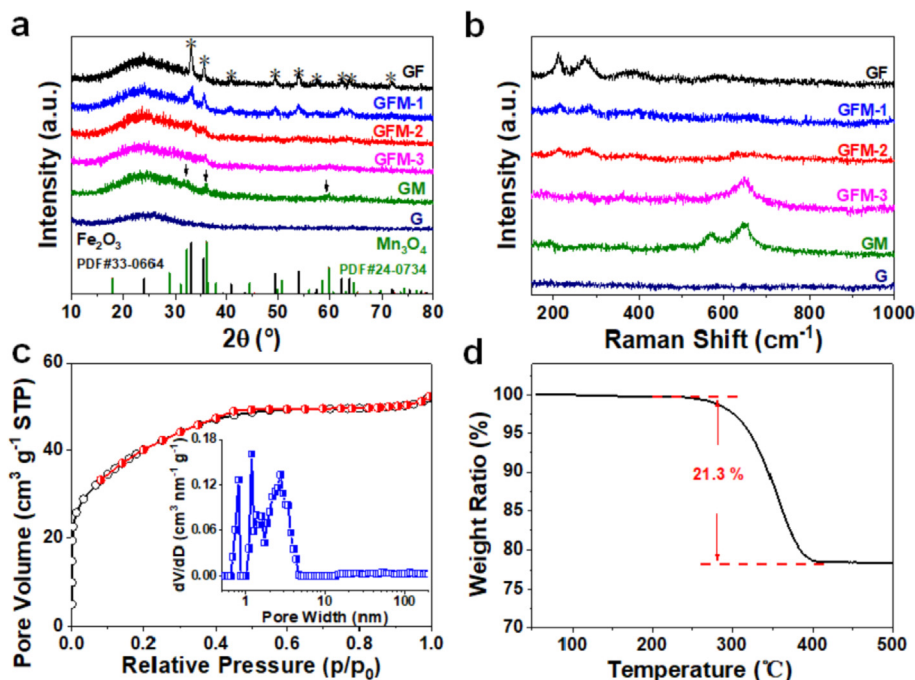


Fig. 2. (a) XRD patterns and (b) Raman spectra of the GFM series composites; (c) N₂ adsorption-desorption isotherms and pore-size distribution curve; and (d) TGA curve of the GFM-2 composite.

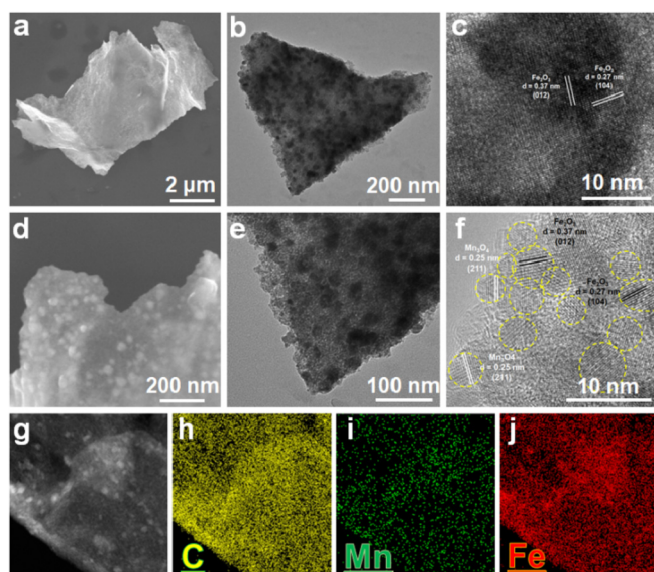


Fig. 3. (a,d) SEM, (b,e) TEM and (f) HRTEM images, as well as (g) the selected region image of GFM-2 with the responding EDXS elements mapping of (h) C, (i) Mn and (j) Fe.

accelerated, which facilitates the further reaction, and thus improves the electrode electrochemical performance, especially at the high rate conditions.

The distribution and lattice structure of Fe₂O₃/Mn₃O₄ in the GFM-2 composite were further characterized by HRTEM (Fig. 3c). The metal oxide nanoparticles with the size of about 20 nm on the rGO nanosheets were observed. The lattice fringes were clear and complete, and the measured fringes spacing was mainly 0.37 and 0.27 nm, which corresponded to the (012) and (104) crystal planes of hematite-type Fe₂O₃, respectively [40,46], showing that the

composition of the metal oxide nanoparticles was principally well-crystallized Fe₂O₃. Further enlarged HRTEM image of GFM-2 is presented in Fig. 3f. There were many well crystallized oxides (marked by yellow dashed line) on rGO with size of only 3–5 nm. These nanocrystals were densely and uniformly distributed and the lattice strips were analyzed. These nanoparticles belong to the hausmannite-type Mn₃O₄ with (211) crystal plane (0.25 nm lattice spacing) [47,48] and Fe₂O₃. The two oxide crystals were independent but next to each other. Such small nanocrystals are conducive to fully increase the exposure of active sites of the metal oxide nanocrystals. Carbon structure patterns of the rGO nanosheets could be also clearly observed at the edge region, which indicates that the lamellar structure of graphene has been retained after oxidation, metal oxides nanocrystals growth and reduction treatment. The rGO sheet was closely bound to metal oxide nanocrystals via densely growing on its surface. Graphene skeleton may be used as an electron transport channel of the composite. Small size greatly reduces the transmission path and resistance of electrons for the metal oxides. Thus, electrons can quickly transfer to the adsorbed lithium polysulfides and promote the further redox reaction.

EDXS was used to analyze the element distribution in GFM-2 (Fig. 3g–j). Both Fe and Mn showed elemental responses, and the distribution images are consistent with the morphology of nanolamellae. The uniform distribution of C atoms is related to that of graphene as the host of the composite. Graphene maintained sufficient integrity and penetrated the whole nanosheet structure, which are helpful for providing sufficient electrons. The uniform distributions of Mn and Fe without obvious aggregation indicate that Mn and Fe are mainly loaded in the form of small-sized nanocrystals. In terms of element content, the atomic content of Fe (22.1%) is about 12 times that of Mn (1.8%), which may be due to the different growth mechanisms of the two oxides. Fe can grow and adhere to the GO surface by hydrolysis, while Mn may only adhere to the GO surface by redox reaction between KMnO₄ and GO nanosheets. The graphene skeleton preservation indicates that the

degree of redox reaction is relatively low, thus the loading content of Mn_3O_4 is much lower than that of Fe_2O_3 . Combined the rGO mass of 21.3 wt% from TGA, the composition of GFM-2 is $\text{rGO} \cdot 0.26\text{Fe}_2\text{O}_3 \cdot 0.014\text{Mn}_3\text{O}_4$.

The chemical state of elements in GFM-2 was characterized by XPS. The response of C, O, Mn and Fe elements can be detected in the survey scan and high-resolution C 1s, Fe 2p and Mn 2p spectra (Fig. 4). C 1s orbital response band can be divided into sp^2 hybrid carbon (284.8 eV) corresponding to C–C/C=C bonds attributing to graphene hexagonal skeleton, C–O (286.2 eV) and O–C=O (288.6 eV) [49,50]. The Fe $2\text{p}_{1/2}$ orbital response bands at 725.4 and 723.9 eV and $2\text{p}_{3/2}$ orbital response bands at 711.5 and 710.5 eV indicate the existence of Fe_2O_3 [51,52]. The Mn $2\text{p}_{1/2}$ orbital response band at 653.2 eV and $2\text{p}_{3/2}$ orbital response band at 641.3 eV also prove that Mn exists in the form of Mn_3O_4 [53]. Li_2S_4 -adsorbed GFM-2 was also characterized as the dash lines shown in Fig. 4c and d, where the peaks obviously shift towards lower energy levels, proving the effective interaction between oxides nanoparticles and polysulfides [54]. The charge transfers between $\text{Fe}_2\text{O}_3/\text{Mn}_3\text{O}_4$ and polysulfides may profit the conversion of polysulfides weakening the shuttle effect.

3.2. Electrochemical properties the GFM modified cathodes

CV tests were carried out for the sole S/G cathode and the modified S/G Li–S battery cathode by mixing S/G and GFM-2 additive with a mass ratio of 20: 1 (S/G + GFM-2), respectively (Fig. 5a). Both electrodes exhibited two reduction peaks corresponding to the reduction of S_8 to Li_2S_x ($4 \leq x \leq 8$) and further reduction to $\text{Li}_2\text{S}_2/\text{Li}_2\text{S}$, as well as corresponding oxidation peaks for the reverse reaction [55,56]. Compared to the S/G electrode, the current response of redox peaks in the CV curve for the mixed S/G + GFM-2 electrode was stronger, which indicates that its capacity is higher. The sharper peak shape indicates that the electrode

reaction rate is faster. The oxidation peak shifted from 2.36 to 2.31 V, and the reduction peaks shifted from 2.01/2.27 to 2.04/2.32 V, respectively. It shows that the GFM-2 composite significantly improves the kinetics of electrode reactions and reduces the polarization degree.

Galvanostatic charge-discharge tests were carried out at the scan rate of 0.1C, and the plots were compared as shown in Fig. 5b. The discharge capacity of the mixed S/G + GFM-2 electrode was $1442.1 \text{ mAh g}^{-1}$, which is larger than $1049.5 \text{ mAh g}^{-1}$ of the S/G electrode. Moreover, the capacity of the first discharge platform corresponding to reduction from S_8 to Li_2S_x ($4 \leq x \leq 8$) was increased by 125.3 mAh g^{-1} , and the capacity of the second discharge platform corresponding to further reduction to $\text{Li}_2\text{S}_2/\text{Li}_2\text{S}$ was increased by 252.6 mAh g^{-1} , indicating that the GFM-2 composite additive plays significant roles for effectively adsorbing lithium polysulfides, reducing the capacity loss caused by shuttle effect to increase the capacity. On the one hand, the adsorption active surface can be well exposed by the uniform and dense distribution of Fe/Mn oxide small nanocrystals. Besides, it can promote the further reaction of adsorbing lithium polysulfides and improve the conversion rate through the rapid electron transport between graphene skeleton and small oxide nanocrystals. The voltage difference (ΔV) between charge and discharge platforms of the two kinds of electrodes was measured. From the sole S/G to mixed S/G + GFM-2 electrodes, the ΔV value decreased from 189 to 167 mV, which indicates that the GFM-2 composite additive could significantly promote the high efficiency of electrode reaction and reduce electrode polarization, consisting with the CV analyses.

Series of GFM composites with different ratios of $\text{Fe}_2\text{O}_3/\text{Mn}_3\text{O}_4$ were obtained as the additives of Li–S battery cathodes to optimize the ratio of iron and manganese oxides in the composites and sole S/G cathode was also used for comparison. The discharging capacity values at different rate conditions are shown in Fig. 5c. The average specific capacities of S@G cathode were 973.3, 819.8, 736.0, 669.3

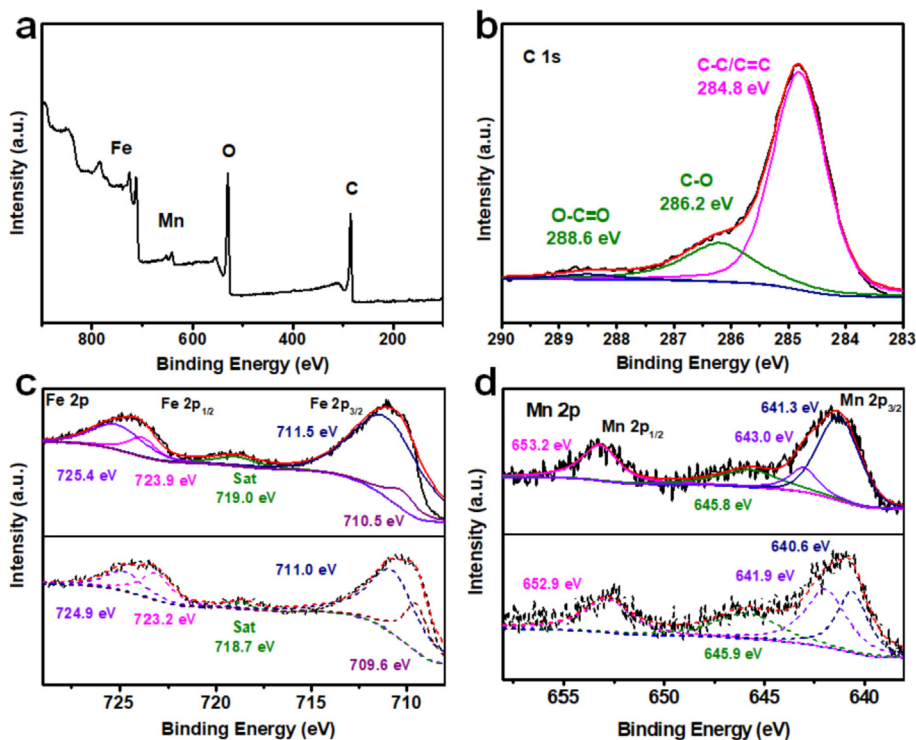


Fig. 4. (a) XPS survey scan and the high-resolution (b) C 1s, (c) Fe 2p and (d) Mn 2p spectra of GFM-2. The dash lines in (c) and (d) stand for the high-resolution Fe 2p and Mn 2p spectra of Li_2S_4 -adsorbed GFM-2, respectively.

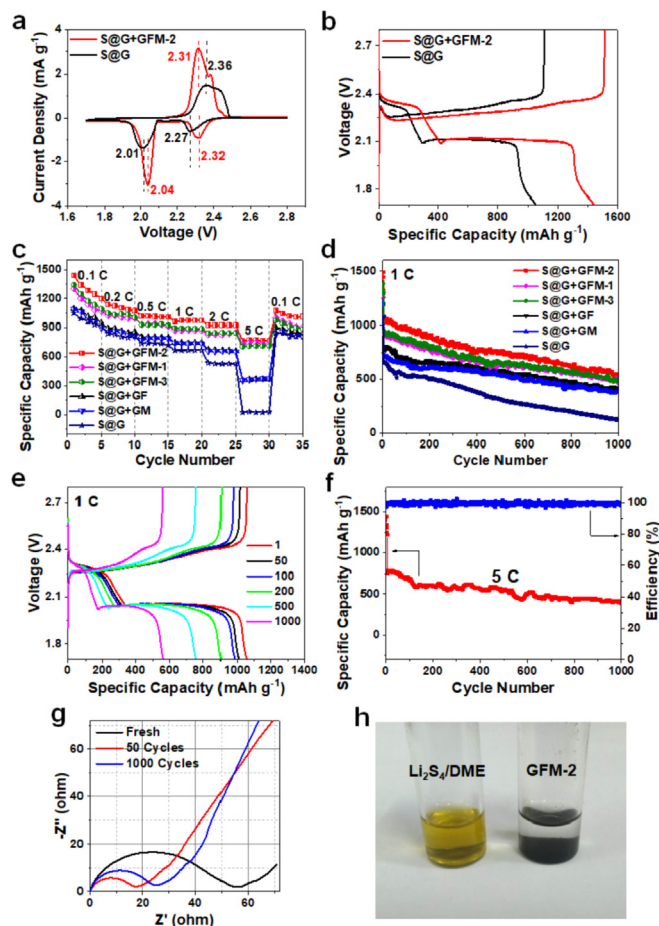


Fig. 5. (a) CV and (b) galvanostatic charge-discharge curves of the first cycle of the S@G and mixed S@G + GFM-2 cathodes; (c) rate performance and (d) cycle performance at 1C of the GFM series composites modified cathodes; (e) galvanostatic charge-discharge profiles at different cycles of the mixed S@G + GFM-2 cathode at 1C; (f) the cycle performance of the mixed S@G + GFM-2 cathode at 5C; (g) EIS curves at different cycles of the mixed S@G + GFM-2 cathode; and (h) the optical photo of visible adsorption experiment.

and 531.1 mAh g^{-1} at 0.1, 0.2, 0.5, 1 and 2C, respectively. When the scan rate was increased to 5C, the average specific capacity of the S@G cathode was only about 20 mAh g^{-1} . As to the mixed S/G + GFM series composite electrodes, the discharging capacities increased significantly, even though there were some differences in the enhancement of electrode performance among the GFM materials with different $\text{Fe}_2\text{O}_3/\text{Mn}_3\text{O}_4$ ratios, especially the two materials using Fe_2O_3 or Mn_3O_4 as the adsorption active materials alone which showed the low effects for performance enhancement. The best performance is achieved with GFM-2 when the reaction source ratio of FeCl_3 and KMnO_4 comes to 1: 1. The discharge specific capacities of the mixed S/G + GFM-2 cathode at 0.1–5 C can reach 1356.3, 1184.4, 1013.5, 972.7, 926.9 and 770.2 mAh g^{-1} , respectively. Thus, the GFM composites can inhibit the loss of active material caused by the lithium polysulfide shuttle effect, increase the polysulfide content conversion, especially at the fast charging-discharging process, which are due to that the small metal oxides uniformly and densely grown on the carbon skeleton have the ability of highly-efficient adsorption, fast electron transport and material transformation.

Cyclic stabilities of the corresponding mixed S/G and series GFM Li–S battery cathodes were tested at 1C (Fig. 5d). The S/G + GFM-2 electrode showed the best performance. The initial capacity of the

mixed S/G + GFM-2 electrode was 1053.5 mAh g^{-1} at 1C and the specific capacity was maintained at 530.1 mAh g^{-1} after 1000 cycles with the average capacity decay rate of each cycle of 0.049%. In contrast, the initial capacity of the sole S@G electrode was only 655.1 mAh g^{-1} . After 1000 cycles, the final specific capacity was 122.6 mAh g^{-1} with the average capacity decay rate of each cycle of 0.081%. Galvanostatic charge-discharge plots of the mixed S/G + GFM-2 electrode in 1000 cycles at 1C are given in Fig. 5e. Although there was certain capacity attenuation, the charging-discharging platforms were stably kept, indicating that the mixed S/G + GFM-2 electrode was stable after the long cycles. A good specific capacity of 400 mAh g^{-1} may be obtained for the mixed S/G + GFM electrode after 1000 cycles at the enhanced scan rate of 5C (Fig. 5f) with the Coulomb efficiency of above 95% throughout the cycles, which proves that the mixed S/G + GFM-2 electrode can achieve efficient reversible energy storage and long usage even under rapid charging-discharging condition.

EIS test of the mixed S@G + GFM-2 electrode at different cycles is shown in Fig. 5g. The charge transfer resistance (R_{ct}) in the initial electrode was 55.6 Ω . After 50 cycles, the R_{ct} value decreased to 17.3 Ω . After 1000 cycles, it increased slightly to 25 Ω . The impedance reduction at the beginning of the cycle is due to optimization of the distribution of active material on the surface of the material after charging and discharging cycles, while the subsequent increase is due to the irreversible deposition of a small amount of $\text{Li}_2\text{S}_2/\text{Li}_2\text{S}$. The straight line in the low frequency region represents the ion diffusion impedance (W_0) in the electrode, which is mainly caused by the ion gradient concentration at the electrolyte/electrode interface. Along with the charging-discharging cycles, the slope of the straight line increased, which means that the ion diffusion is easier to proceed because of the more sufficient electrolyte infiltration. For further illustrating the adsorption capacity of GFM-2 composite for polysulfides, $\text{Li}_2\text{S}_4/\text{DME}$ solution was used for adsorption experiment. Optical photos (Fig. 5h) show that after adding GFM-2 composite, the color of lithium polysulfide solution has completely turned colorless after oscillation and static precipitation for 5 min, indicating the strong adsorption capacity of the composite for polysulfides. The high specific surface area exposed by small-sized oxide nanocrystals maximizes the chemical adsorption effect of oxide materials.

In order to meet the practical needs of Li–S batteries, it is very important to further improve the energy density of the battery system. Therefore, it is necessary to reduce the amount of non-active substances in the battery as much as possible [57,58]. In this work, the performances of the GFM-2 modified electrode with insufficient amount of electrolyte were explored. The ratio of electrolyte/sulfur was adjusted to E/S = 15 and 8 $\text{mL g}_\text{S}^{-1}$, respectively. Rate and cycle performance tests were carried out (Fig. 6a). The Li–S battery of the GFM-2 modified composite cathode released 1308.0, 1036.6 and 928.6 mAh g^{-1} at 0.1, 0.2 and 0.5C, respectively, when the E/S value was 15 $\text{mL g}_\text{S}^{-1}$. After 250 cycles, the capacity retention rate was 88.7%. When the E/S value was further reduced to 8 $\text{mL g}_\text{S}^{-1}$, the discharge specific capacity at 0.1, 0.2 and 0.5C could reach 1230.4, 1019.5 and 904.2 mAh g^{-1} , respectively. The capacity retention reached 80.3% after 250 cycles. The areal sulfur loading on electrode is also one of the important indicators for the practical application of Li–S batteries. When the sulfur loading for the GFM-2 modified cathode was increased to 2.8 mg cm^{-2} , meanwhile, the proportion of electrolyte was reduced to E/S = 10 $\text{mL g}_\text{S}^{-1}$ (Fig. 6b), the specific discharge capacities of the battery could reach 1163.6, 882.5 and 777.5 mAh g^{-1} at 0.1, 0.2 and 0.5C, respectively. When the scan rate was increased to 1C, at the beginning the capacity of the battery decreased obviously, which indicates the electrolyte is in an insufficient state, while, after a certain charging-discharging cycles the specific capacity of the

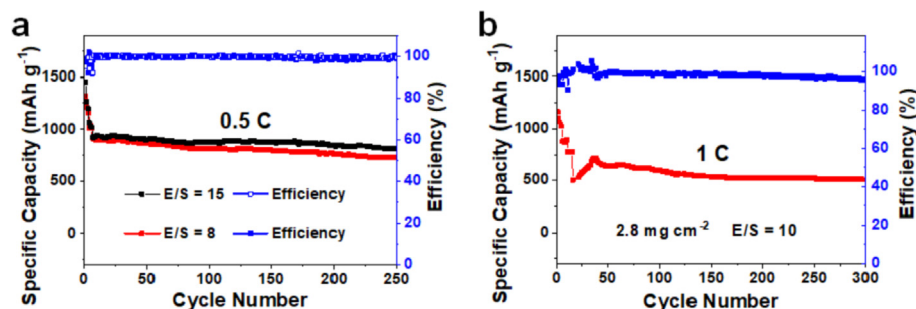


Fig. 6. (a) Rate and cycle performances of the GFM-2 modified cathode under $E/S = 15$ and 8 mL g^{-1} ; and (b) the GFM-2 modified cathode electrochemical performance with the sulfur loading of 2.8 mg cm^{-2} under $E/S = 10 \text{ mL g}^{-1}$.

Table 1

Performance comparison with recently reported Li–S batteries.

Cathode	$E/S \text{ (mL g}^{-1}\text{)}$	Capacity (mAh g^{-1})	Cycle Number	Retention (%)	Ref.
SPPyMnO ₂	5	1367 (0.2C)	500	74	[59]
MoP-CNT-S	4	830 (0.1C)	50	—	[60]
Mo ₆ S ₈ -S@Fe ₃ O ₄ -NC	4.2	1050 (0.15C)	300	80	[61]
Fe/Co-N@C/S	5	1296 (0.04C)	100	—	[62]
S@CNTs/Co ₃ S ₄ @NC	5	1577 (0.1C)	1000	—	[63]
Co,N-CNTs-CNS/CFC	6.94	727.5 (0.1C)	70	—	[64]
C/TiO ₂ -TiN/S	6.8	640 (0.1C)	400	79	[65]
CoCp2	4.7	1148 (0.1C)	20	—	[66]
S@G + GFS-2	8	1230.4 (0.1C)	250	80.3	Our work
	10	1163.6 (0.1C)	300	70.9	

battery could be stabilized at 716.5 mAh g^{-1} , and after 300 cycles the specific capacity was still maintained at 507.9 mAh g^{-1} , which indicates that the GFM-2 modified cathode may achieve high specific capacity and more stable cycle capacity under the high loading and low electrolyte dosage conditions. These prove the potential application prospects of this material in the practical process of Li–S batteries. Compared to state-of-the-art Li–S batteries operated at low E/S ratios (Table 1) [59–66], our work shows comparable high capacitance and cyclic stability.

4. Conclusions

The novel GFM-2 composite has been successfully prepared, where well dispersed 20 nm particles composing of 3–5 nm $\text{Fe}_2\text{O}_3/\text{Mn}_3\text{O}_4$ binary crystals may be uniformly distributed on the rGO nanosheets. The choice of GO precursor is advisable for the synthesis of GFM series composites. The lamellar topologic structure of GO with the structural defects can result in a relatively large specific surface area. The oxygen-containing functional groups including hydroxyl groups, carboxyl groups and oxygen bridges in the honeycomb-type carbon atom skeleton may lead to the electronegative characteristic of the GO surface, which is easy to adsorb Fe^{3+} ions. The large specific surface area and the ultrasound treatment as well as the relatively low temperatures (90 and 350°C) reaction processes ensure that the adsorbed ions and the subsequent resultant metal oxides nanoparticles more uniformly distributed on the lamellar surface. Besides, KMnO_4 can not only oxidize carbon skeleton forming Mn_3O_4 nanocrystals, but also result in more carbon skeleton defects at the same time. Thus, the graphene/oxides composites have abundant micro/mesopores with a high specific surface area, which overcomes the shortcomings of high phase density and low specific surface area of metal oxides. It can maximize the adsorption active sites of oxides for lithium polysulfides, improve polysulfides immobilization ability and

inhibit shuttle effect. Graphene skeleton may rapidly transmit electrons. The metal oxide nanocrystals shorten the electron transport path and accelerate the further reaction of the adsorbed lithium polysulfides. The micro/mesoporous structure can also accommodate sulfur physically. Overall, high reversible capacities may be obtained for the modified sulfur@graphene cathode with mixed very low amount of GFM-2 additive under different electrolyte dosages and sulfur loading amounts, indicating a possible component design scheme for the practical Li–S batteries sulfur cathode modification.

Declaration of competing interest

The authors declare that they have no known competing financial interests or personal relationships that could have appeared to influence the work reported in this paper.

CRediT authorship contribution statement

Hang Zhang: Formal analysis, Methodology, Writing - original draft. **Qiuming Gao:** Formal analysis, Funding acquisition, Investigation, Methodology, Supervision, Writing - original draft, Writing - review & editing. **Zeyu Li:** Formal analysis. **Peng Xu:** Formal analysis. **Hong Xiao:** Formal analysis. **Tengfei Zhang:** Formal analysis. **Xiao Liang:** Formal analysis.

Acknowledgment

This work was supported by National Science Foundation, China (No. 21571010 and U0734002), National Basic Research Programs, China (973 Program, No. 2014CB931800 and 2011CB935700), Aeronautic Project, China (No. 2013ZF51069) and 111 Project, China (No. B14009).

References

- [1] Q. Zhang, F. Li, J.-Q. Huang, H. Li, Lithium-sulfur batteries: Co-existence of challenges and opportunities, *Adv. Funct. Mater.* 28 (2018), 1804589.
- [2] Z.-W. Zhang, H.-J. Peng, M. Zhao, J.-Q. Huang, Heterogeneous/homogeneous mediators for high-energy-density lithium-sulfur batteries: progress and prospects, *Adv. Funct. Mater.* 28 (2018), 1707536.
- [3] M. Rana, S.A. Ahad, M. Li, B. Luo, L. Wang, I. Gentle, R. Knibbe, Review on areal capacities and long-term cycling performances of lithium sulfur battery at high sulfur loading, *Energy Storage Mater.* 18 (2019) 289–310.
- [4] R. Kumar, J. Liu, J.-Y. Hwang, Y.-K. Sun, Recent Research trends in Li-S batteries, *J. Mater. Chem. A* 6 (2018) 11582–11605.
- [5] Y. Liu, P. He, H. Zhou, Rechargeable solid-state Li-air and Li-S batteries: materials, construction, and challenges, *Adv. Energy Mater.* 8 (2018), 1701602.
- [6] W. Guo, Y. Fu, A perspective on energy densities of rechargeable Li-S batteries and alternative sulfur-based cathode materials, *Energy Environ. Mater.* 1 (2018) 20–27.
- [7] H. Xu, Y. Liu, Q. Bai, R. Wu, Discarded cigarette filter-derived hierarchically porous Carbon@Graphene composites for lithium-sulfur batteries, *J. Mater. Chem. A* 7 (2019) 3558–3562.
- [8] S. Rehman, X. Gu, K. Khan, N. Mahmood, W. Yang, X. Huang, S. Guo Y. Hou, 3D vertically aligned and interconnected porous carbon nanosheets as sulfur immobilizers for high performance lithium-sulfur batteries, *Adv. Energy Mater.* 6 (2016), 1502518.
- [9] L. Du, Q. Wu, L. Yang, X. Wang, R. Che, Z. Lyu, W. Chen, X. Wang, Z. Hu, Efficient synergism of electrocatalysis and physical confinement leading to durable high-power lithium-sulfur batteries, *Nano Energy* 57 (2019) 34–40.
- [10] G. Zhou, Y. Zhao, A. Manthiram, Dual-confined flexible sulfur cathodes encapsulated in nitrogen-doped double-shelled hollow carbon spheres and wrapped with graphene for Li-S batteries, *Adv. Energy Mater.* 5 (2015) 1402263.
- [11] H. Pan, J. Chen, R. Cao, V. Murugesan, N.N. Rajput, K.S. Han, K. Persson, L. Estevez, M.H. Engelhard, J.-G. Zhang, K.T. Mueller, Y. Cui, Y. Shao, J. Liu, Non-encapsulation approach for high performance Li-S batteries through controlled nucleation and growth, *Nat. Energy* 2 (2017) 813–820.
- [12] S.H. Chung, A. Manthiram, Designing lithium-sulfur batteries with high-loading cathodes at a lean electrolyte condition, *ACS Appl. Mater. Interfaces* 10 (2018) 43749–43759.
- [13] W. Cai, G. Li, D. Luo, G. Xiao, S. Zhu, Y. Zhao, Z. Chen, Y. Zhu, Y. Qian, The dual-play of 3D conductive scaffold embedded with Co, N codoped hollow polyhedra toward high-performance Li-S full cell, *Adv. Energy Mater.* 8 (2018) 1802561.
- [14] C. Fu, M.B. Oviedo, Y. Zhu, A. von Wald Cresce, K. Xu, G. Li, M.E. Itkis, R.C. Haddon, M. Chi, Y. Han, B.M. Wong, J. Guo, Confined lithium-sulfur reactions in narrow-diameter carbon nanotubes reveal enhanced electrochemical reactivity, *ACS Nano* 12 (2018) 9775–9784.
- [15] Y. Yuan, G. Tan, J. Wen, J. Lu, L. Ma, C. Liu, X. Zuo, R. Shahbazian-Yassar, T. Wu, K. Amine, Encapsulating various sulfur allotropes within graphene nanocages for long-lasting lithium storage, *Adv. Funct. Mater.* 28 (2018), 1706443.
- [16] L. Kong, B.-Q. Li, H.-J. Peng, R. Zhang, J. Xie, J.-Q. Huang, Q. Zhang, Porphyrin-derived graphene-based nanosheets enabling strong polysulfide chemisorption and rapid kinetics in lithium-sulfur batteries, *Adv. Energy Mater.* 8 (2018), 1800849.
- [17] D. Cheng, P. Wu, J. Wang, X. Tang, T. An, H. Zhou, D. Zhang, T. Fan, Synergetic pore structure optimization and nitrogen doping of 3D porous graphene for high performance lithium sulfur battery, *Carbon* 143 (2019) 869–877.
- [18] H. Wang, B.D. Adams, H. Pan, L. Zhang, K.S. Han, L. Estevez, D. Lu, H. Jia, J. Feng, J. Guo, K.P. Zavadil, Y. Shao, J.-G. Zhang, Tailored reaction route by micropore confinement for Li-S batteries operating under lean electrolyte conditions, *Adv. Energy Mater.* 8 (2018), 1800590.
- [19] J.-G. Wang, K. Xie, B. Wei, Advanced engineering of nanostructured carbons for lithium-sulfur batteries, *Nano Energy* 15 (2015) 413–444.
- [20] S. Wu, R. Ge, M. Lu, R. Xu, Z. Zhang, Graphene-based nano-materials for lithium-sulfur battery and sodium-ion battery, *Nano Energy* 15 (2015) 379–405.
- [21] S.-H. Chung, C.-H. Chang, A. Manthiram, Progress on the critical parameters for lithium-sulfur batteries to be practically viable, *Adv. Funct. Mater.* 28 (2018), 1801188.
- [22] Y. Wang, X. Huang, S. Zhang, Y. Hou, Sulfur hosts against the shuttle effect, *Small Methods* 2 (2018) 1700345.
- [23] M.-Q. Zhao, X.-F. Liu, Q. Zhang, G.-L. Tian, J.-Q. Huang, W. Zhu, F. Wei, Graphene/single-walled carbon nanotube hybrids: one-step catalytic growth and applications for high-rate Li-S batteries, *ACS Nano* 6 (2012) 10759–10769.
- [24] C. Tang, Q. Zhang, M.Q. Zhao, J.Q. Huang, X.B. Cheng, G.L. Tian, H.J. Peng, F. Wei, Nitrogen-doped aligned carbon nanotube/graphene sandwiches: facile catalytic growth on bifunctional natural catalysts and their applications as scaffolds for high-rate lithium-sulfur batteries, *Adv. Mater.* 26 (2014) 6100–6105.
- [25] M.Q. Zhao, Q. Zhang, J.Q. Huang, G.L. Tian, J.Q. Nie, H.J. Peng, F. Wei, Unstacked double-layer templated graphene for high-rate lithium-sulphur batteries, *Nat. Commun.* 5 (2014) 3410.
- [26] X. Liang, C.Y. Kwok, F. Lodi-Marzano, Q. Pang, M. Cuisinier, H. Huang, C.J. Hart, D. Houtarde, K. Kaup, H. Sommer, T. Brezesinski, J. Janek, L.F. Nazar, Tuning transition metal oxide-sulfur interactions for long life lithium sulfur batteries: the “goldilocks” principle, *Adv. Energy Mater.* 6 (2016), 1501636.
- [27] Q. Zhang, Y. Wang, Z.W. Seh, Z. Fu, R. Zhang, Y. Cui, Understanding the anchoring effect of two-dimensional layered materials for lithium-sulfur batteries, *Nano Lett.* 15 (2015) 3780–3786.
- [28] J.-Y. Hwang, H.M. Kim, S.-K. Lee, J.-H. Lee, A. Abouimrane, M.A. Khaleel, I. Belharouak, A. Manthiram, Y.-K. Sun, High-energy, high-rate, lithium-sulfur batteries: synergetic effect of hollow TiO₂-webbed carbon nanotubes and a dual functional carbon-paper interlayer, *Adv. Energy Mater.* 6 (2016), 1501480.
- [29] Y. Sun, N. Liu, Y. Cui, Promises and challenges of nanomaterials for lithium-based rechargeable batteries, *Nat. Energy* 1 (2016) 16071.
- [30] X. Liu, J.Q. Huang, Q. Zhang, L. Mai, Nanostructured metal oxides and sulfides for lithium-sulfur batteries, *Adv. Mater.* 29 (2017), 1601759.
- [31] Y. Zhu, S. Wang, Z. Miao, Y. Liu, S.L. Chou, Novel non-carbon sulfur hosts based on strong chemisorption for lithium-sulfur batteries, *Small* 14 (2018), 1801987.
- [32] Q. Pang, D. Kundu, L.F. Nazar, A graphene-like metallic cathode host for long-life and high-loading lithium-sulfur batteries, *Mater. Horiz.* 3 (2016) 130–136.
- [33] Q. Lin, J. Zhang, D. Kong, T. Cao, S.-W. Zhang, X. Chen, Y. Tao, W. Lv, F. Kang, Q.-H. Yang, Deactivating defects in graphenes with Al₂O₃ nanoclusters to produce long-life and high-rate sodium-ion batteries, *Adv. Energy Mater.* 9 (2019), 1803078.
- [34] Q. Gong, Y. Wang, Q. Hu, J. Zhou, R. Feng, P.N. Duchesne, P. Zhang, F. Chen, N. Han, Y. Li, C. Jin, Y. Li, S.T. Lee, Ultrasmall and phase-pure W₂C nanoparticles for efficient electrocatalytic and photoelectrochemical hydrogen evolution, *Nat. Commun.* 7 (2016) 13216.
- [35] Z. Chen, R. Wu, M. Liu, H. Wang, H. Xu, Y. Guo, Y. Song, F. Fang, X. Yu, D. Sun, General synthesis of dual carbon-confined metal sulfides quantum dots toward high-performance anodes for sodium-ion batteries, *Adv. Funct. Mater.* 27 (2017), 1702046.
- [36] Y. Wang, W. Lai, N. Wang, Z. Jiang, X. Wang, P. Zou, Z. Lin, H.J. Fan, F. Kang, C.-P. Wong, C. Yang, A reduced graphene oxide/mixed-valence manganese oxide composite electrode for tailorable and surface mountable supercapacitors with high capacitance and super-long life, *Energy Environ. Sci.* 10 (2017) 941–949.
- [37] X. Liang, C. Hart, Q. Pang, A. Garsuch, T. Weiss, L.F. Nazar, A highly efficient polysulfide mediator for lithium-sulfur batteries, *Nat. Commun.* 6 (2015) 5682.
- [38] W. Tian, Q. Gao, Y. Tan, Y. Zhang, J. Xu, Z. Li, K. Yang, L. Zhu, Z. Liu, Three-dimensional functionalized graphenes with systematic control over the interconnected pores and surface functional groups for high energy performance supercapacitors, *Carbon* 85 (2015) 351–362.
- [39] J. Zhao, Y.-Z. Zhang, F. Zhang, H. Liang, F. Ming, H.N. Alshareef, Z. Gao, Partially reduced holey graphene oxide as high performance anode for sodium-ion batteries, *Adv. Energy Mater.* 9 (2019), 1803215.
- [40] H. Zhang, Q. Gao, K. Yang, Y. Tan, W. Tian, L. Zhu, Z. Li, C. Yang, Solvothermally induced α -Fe₂O₃/graphene nanocomposites with ultrahigh capacitance and excellent rate capability for supercapacitors, *J. Mater. Chem. A* 3 (2015) 22005–22011.
- [41] H. Xia, C. Hong, B. Li, B. Zhao, Z. Lin, M. Zheng, S.V. Savilov, S.M. Aldoshin, Facile synthesis of hematite quantum-dot/functionalized graphene-sheet composites as advanced anode materials for asymmetric supercapacitors, *Adv. Funct. Mater.* 25 (2015) 627–635.
- [42] J. Duan, S. Chen, S. Dai, S.Z. Qiao, Shape control of Mn₃O₄ nanoparticles on nitrogen-doped graphene for enhanced oxygen reduction activity, *Adv. Funct. Mater.* 24 (2014) 2072–2078.
- [43] J.G. Wang, D. Jin, R. Zhou, X. Li, X.R. Liu, C. Shen, K. Xie, B. Li, F. Kang, B. Wei, Highly flexible graphene/Mn₃O₄ nanocomposite membrane as advanced anodes for Li-ion batteries, *ACS Nano* 10 (2016) 6227–6234.
- [44] J. Hou, C. Cao, F. Idrees, X. Ma, Hierarchical porous nitrogen-doped carbon nanosheets derived from silk for ultrahigh-capacity battery anodes and supercapacitors, *ACS Nano* 9 (2015) 2556–2564.
- [45] G. Li, J. Sun, W. Hou, S. Jiang, Y. Huang, J. Geng, Three-dimensional porous carbon composites containing high sulfur nanoparticle content for high-performance lithium-sulfur batteries, *Nat. Commun.* 7 (2016) 10601.
- [46] C. Zheng, S. Niu, W. Lv, G. Zhou, J. Li, S. Fan, Y. Deng, Z. Pan, B. Li, F. Kang, Q.-H. Yang, Propelling polysulfides transformation for high-rate and long-life lithium-sulfur batteries, *Nano Energy* 33 (2017) 306–312.
- [47] A. Ejigu, M. Edwards, D.A. Walsh, Synergistic catalyst-support interactions in a graphene-Mn₃O₄ electrocatalyst for vanadium redox flow batteries, *ACS Catal.* 5 (2015) 7122–7130.
- [48] S. Li, L.L. Yu, Y.T. Shi, J. Fan, R.B. Li, G.D. Fan, W.L. Xu, J.T. Zhao, Greatly enhanced faradic capacities of 3D porous Mn₃O₄/G composites as lithium-ion anodes and supercapacitors by C-O-Mn bonding, *ACS Appl. Mater. Interfaces* 11 (2019) 10178–10188.
- [49] N.R. Kim, S.M. Lee, M.W. Kim, H.J. Yoon, W.G. Hong, H.J. Kim, H.J. Choi, H.-J. Jin, Y.S. Yun, Amphicharge-storable pyropolymers containing multitiered nanopores, *Adv. Energy Mater.* 7 (2017), 1700629.
- [50] H. Wang, P. Hu, J. Yang, G. Gong, L. Guo, X. Chen, Renewable-juglone-based high-performance sodium-ion batteries, *Adv. Mater.* 27 (2015) 2348–2354.
- [51] L. Liu, X. Yang, C. Lv, A. Zhu, X. Zhu, S. Guo, C. Chen, D. Yang, Seaweed-derived route to Fe₂O₃ hollow nanoparticles/N-doped graphene aerogels with high lithium ion storage performance, *ACS Appl. Mater. Interfaces* 8 (2016) 7047–7053.
- [52] L. Liu, J. Lang, P. Zhang, B. Hu, X. Yan, Facile synthesis of Fe₂O₃ nano-Dots@Nitrogen-doped graphene for supercapacitor electrode with ultralong cycle

- life in KOH electrolyte, *ACS Appl. Mater. Interfaces* 8 (2016) 9335–9344.
- [53] Y. Chu, L. Guo, B. Xi, Z. Feng, F. Wu, Y. Lin, J. Liu, D. Sun, J. Feng, Y. Qian, S. Xiong, Embedding $\text{MnO@Mn}_3\text{O}_4$ nanoparticles in an N-Doped-Carbon framework derived from Mn-organic clusters for efficient lithium storage, *Adv. Mater.* 30 (2018), 1704244.
- [54] J. Guo, X. Zhang, X. Du, F. Zhang, A Mn_3O_4 nano-wall array based binder-free cathode for high performance lithium-sulfur batteries, *J. Mater. Chem. A* 5 (2017) 6447.
- [55] C. Zu, A. Manthiram, Hydroxylated graphene-sulfur nanocomposites for high-rate lithium-sulfur batteries, *Adv. Energy Mater.* 3 (2013) 1008–1012.
- [56] L. Qie, A. Manthiram, A facile layer-by-layer approach for high-areal-capacity sulfur cathodes, *Adv. Mater.* 27 (2015) 1694–1700.
- [57] X.-B. Cheng, J.-Q. Huang, H.-J. Peng, J.-Q. Nie, X.-Y. Liu, Q. Zhang, F. Wei, Polysulfide shuttle control: towards a lithium-sulfur battery with superior capacity performance up to 1000 cycles by matching the sulfur/electrolyte loading, *J. Power Sources* 253 (2014) 263–268.
- [58] M. Agostini, J.-Y. Hwang, H.M. Kim, P. Bruni, S. Brutti, F. Croce, A. Matic, Y.-K. Sun, Minimizing the electrolyte volume in Li-S batteries: a step forward to high gravimetric energy density, *Adv. Energy Mater.* 8 (2018), 1801560.
- [59] Y. Ansari, S. Zhang, B. Wen, F. Fan, Y.-M. Chiang, Stabilizing Li-S battery through multilayer encapsulation of sulfur, *Adv. Energy Mater.* 9 (2018), 1802213.
- [60] Y. Yang, Y. Zhong, Q. Shi, Z. Wang, K. Sun, H. Wang, Electrocatalysis in lithium sulfur batteries under lean electrolyte conditions, *Angew. Chem. Int. Ed.* 57 (2018) 15549.
- [61] K. Lu, Y. Liu, J. Chen, Z. Zhang, Y. Cheng, Redox catalytic and quasi-solid sulfur conversion for high capacity lean lithium sulfur batteries, *ACS Nano* 13 (2019) 14540.
- [62] H. Ye, J. Sun, S. Zhang, H. Lin, T. Zhang, Q. Yao, J.Y. Lee, Stepwise electrocatalysis as a strategy against polysulfide shuttling in Li-S batteries, *ACS Nano* 13 (2019) 14208.
- [63] H. Zhang, M. Zou, W. Zhao, Y. Wang, Y. Chen, Y. Wu, L. Dai, A. Cao, Highly dispersed catalytic Co_3S_4 among a hierarchical carbon nanostructure for high rate and long-life lithium-sulfur batteries, *ACS Nano* 13 (2019) 3982.
- [64] D. Fang, Y. Wang, C. Qian, X. Liu, X. Wang, S. Chen, S. Zhang, Synergistic regulation of polysulfides conversion and deposition by MOF-derived hierarchically ordered carbonaceous composite for high-energy lithium-sulfur batteries, *Adv. Funct. Mater.* 29 (2019), 1900875.
- [65] Z.-L. Xu, S.J. Kim, D. Chang, K.-Y. Park, K.S. Dae, K.P. Dao, J.M. Yuk, K. Kang, Visualization of regulated nucleation and growth of lithium sulfides for high energy lithium sulfur batteries, *Energy Environ. Sci.* 12 (2019) 3144.
- [66] M. Zhao, H.-J. Peng, J.-Y. Wei, J.-Q. Huang, B.-Q. Li, H. Yuan, Q. Zhang, Dictating high-capacity lithium-sulfur batteries through redox-mediated lithium sulfide growth, *Small Methods* (2019), 1900344.